Research Square

Preprints are preliminary reports that have not undergone peer review.
They should not be considered conclusive, used to inform clinical practice,
or referenced by the media as validated information.

Structural and functional insights into KIDINS220-mediated regulation of the phosphate exporter XPR1

Zhu Liu

liuzhu@mail.hzau.edu.cn

Huazhong Agricultural University https://orcid.org/0000-0003-4073-7237

Yan Liu

Huazhong Agricultural University

Jie Zhang

Huazhong Agricultural University

Lihuan Jiang

Huazhong Agricultural University

Kun Li

Huazhong Agricultural University

Kangning Tan

Huazhong Agricultural University

Haitao He

Huazhong Agricultural University

Zhangmeng Du

Huazhong Agricultural University

Jiaqi Zuo

Huazhong Agricultural University

Shuo Cao

Huazhong Agricultural University

Xuemei Peng

Huazhong Agricultural University

Guojing Bu

Huazhong Agricultural University

Wenhui Zhang

Huazhong Agricultural University

Yanke Chen

Huazhong Agricultural University https://orcid.org/0000-0002-0344-880X

Yong Wang

Zhejiang University https://orcid.org/0000-0001-9156-0377

Article

Keywords:

Posted Date: August 13th, 2026

DOI: https://doi.org/10.21203/rs.3.rs-10212030/v1

License: This work is licensed under a Creative Commons Attribution 4.0 International License.
Read Full License

Additional Declarations: There is **NO** Competing Interest.

Abstract

XPR1 is the sole known protein that transports inorganic phosphate (Pi) out of cells in metazoans, dynamically regulated by inositol polyphosphates (InsP) signaling and protein interactions to maintain cellular phosphate homeostasis. While InsP-mediated regulation is well-characterized, the mechanistic role of direct protein interactors remains poorly understood. Here, we elucidate the structural and functional interplay between XPR1 and its regulatory partner KIDINS220 using cryo-EM, live-cell FLIM-FRET, and functional transport assays. We demonstrate that KIDINS220 stabilizes an unconventional conformation of the XPR1 SPX domain characterized by a ~ 180° rotation. This rearrangement establishes dual $InsP_6$-anchored interfaces, allosterically repositioning the SPX N-terminus toward the XPR1 C-terminal region and trapping the transporter in an inactive state. FLIM-FRET profiling visualizes and confirms that KIDINS220 promotes a more compact and conformationally homogeneous population of XPR1 in live cells. Under $InsP_6$-bound conditions, KIDINS220 enforces TM9b closure and cytoplasmic C-plug occlusion, obstructing the Pi permeation pathway. Upon Pi sensing, TM9b transitions to an open conformation, yet persistent C-plug engagement—mediated by hydrophobic and electrostatic networks—prevents substrate translocation. Functional validation demonstrates that KIDINS220 suppresses XPR1-mediated Pi transport, establishing its role as a dual-functional regulator: a trafficking chaperone and a membrane-localized brake. We propose a cooperative gating model where Pi acts as both chemical substrate and allosteric trigger to overcome KIDINS220-imposed inhibition. This work defines a tiered regulatory paradigm integrating protein scaffolding, ligand sensing, and dynamic gating for precision control of phosphate homeostasis.

Introduction

Inorganic phosphate (Pi) is an essential nutrient for all living organisms, serving as a fundamental component of nucleic acids, phospholipids, and energy carriers like ATP. To maintain cytosolic Pi level within physiological range required for metabolic homeostasis, human cells have evolved sophisticated transport systems and regulatory networks to control Pi uptake and efflux[1]. Pi import is primarily mediated by high- and low-affinity transporters belonging to the SLC34 and SLC20 families[2–7], while Pi export is facilitated by the XPR1 transporter[8]. These pathways collectively ensure cellular Pi balance in response to varying nutritional states.

Human XPR1 was initially identified as the cell-surface receptor mediating infection by xenotropic and polytropic murine leukemia viruses[9,10]. Subsequently, it was established as the principal phosphate exporter in mammalian cells[8,11]. Dysfunction or loss of XPR1 activity leads to intracellular Pi accumulation, a condition linked to pathological states such as primary familial brain calcification (PFBC) and cancer metabolic reprogramming[12–17]. XPR1's architecture includes an N-terminal SPX domain that binds inositol polyphosphate (InsP) signals[11,18–21] and a transmembrane domain (TMD) facilitating Pi translocation. This transporter's activity is dynamically regulated by InsP signals, particularly inositol hexakisphosphate ($InsP_6$) and its hyperphosphorylated derivatives (PP-$InsP_7$/PP-

$InsP_8$)[22–25], which modulate XPR1 function in response to cellular Pi levels, thereby coupling phosphate export to intracellular phosphate status.

Our[26] and other groups' structural studies[27–34] have elucidated multiple conformational states of human XPR1, revealing key aspects of its transport and regulation mechanisms. Structural analyses demonstrate that InsPs binding induce SPX domain dimerization, stabilizing conformations required for activation[27–29,34]. This signal triggers a cascade of coordinated TMD rearrangements—including TM9b helix reconfiguration[26,27,29,30,34] and C-plug dissociation[27,28,34]—to open the substrate permeation pathway. These results define a dual regulatory mechanism where SPX domain sensing and TMD gating work together for controlled phosphate export. Beyond this intrinsic regulatory machinery, XPR1 function is further subject to modulation by interactions with additional cellular protein partners, such as KIDINS220[16].

Emerging evidence identifies KIDINS220 as a critical regulator of XPR1, controlling its subcellular localization and function to sustain cellular phosphate responsiveness[16]. This scaffold protein, predominantly expressed in neuronal tissues where it mediates survival and maturation pathways[35,36], forms a functional complex with XPR1 that governs cellular phosphate homeostasis[16,37]. Critically, in ovarian cancers, ablation of KIDINS220 disrupts XPR1-mediated phosphate efflux, leading to cytotoxic intracellular phosphate accumulation, which manifests as vacuolization and subsequent cell death[16]. This suggests that targeting the XPR1-KIDINS220 export axis offers a promising anticancer therapeutic approach[16,17,38,39]. However, the underlying molecular mechanism of KIDINS220 in regulating XPR1 function remains unclear.

Here, we sought to elucidate how KIDINS220 modulates XPR1 activity at the molecular level. We determined cryo–EM structures of the KIDINS220-associated XPR1 under signaling-relevant ligand conditions, capturing regulatory conformations in which KIDINS220 stabilizes alternative orientations of the SPX domain and maintains C-plug engagement at the intracellular gate. Structural finding and functional analyses demonstrate that KIDINS220 serves as a negative regulator of XPR1-mediated phosphate export. Together, these findings establish a structural and mechanistic framework illustrating how protein–protein interactions integrate with ligand-dependent control to fine-tune phosphate homeostasis.

Results

Cryo-EM structure of XPR1 bound to KIDINS220 uncovers allosteric regulation

Studies show InsPs regulate XPR1 transport via SPX domain binding[11,18], and KIDINS220 modulates phosphate efflux[16]. To elucidate how KIDINS220 further modulates XPR1 function, we co-expressed both proteins in HEK293F cells for single-particle cryo-EM analysis. Initial attempts using full-length

KIDINS220 yielded insufficient protein quantities for structural determination. Guided by KIDINS220's domain architecture (Supplementary Fig. 1a)—which includes an N-terminal ankyrin-repeats (ARs) domain, a four-helix transmembrane domain (TMD), and cytosolic sterile alpha motif (SAM), kinase interaction motif (KIM), and PDZ domain[36]—we engineered a C-terminally truncated construct lacking the SAM, KIM and PDZ domains (named KIDINS220$^{1-722}$: encompassing residues 1-722,). This KIDINS220$^{1-722}$ variant expressed stably and formed a homogeneous complex with XPR1 suitable for cryo-EM analysis (Supplementary Fig. 1b). This observation suggests that XPR1 primarily engages the AR-TMD region of KIDINS220. AlphaFold3 multimer predictions[40] confirm this: SAM, KIM and PDZ domains were not predicted at the interface, while the AR domain formed the main contact with the XPR1 cytosolic region (Supplementary Fig. 1c).

Cryo-EM analysis of the XPR1-KIDINS220$^{1-722}$ complex, prepared in the presence of $InsP_6$, yielded a dimeric structure at an overall resolution of 3.6 Å (referred to as XPR1^{InsP6} hereafter) (Supplementary Fig. 2, Supplementary Table 1). Well-defined density was observed for the TMD and SPX domains of the XPR1 dimer (Fig. 1a, Supplementary Fig. 3). Weak but discernible extra density was observed surrounding the SPX domains, which likely corresponds to KIDINS220$^{1-722}$ (Fig. 1c), spatially aligned with AlphaFold3-predicted interaction regions (Supplementary Fig. 1c). However, these densities appeared as discontinuous segments distributed across multiple locations (Supplementary Fig. 4a), exhibiting substantial heterogeneity that prevented its structural modeling. The resolved XPR1 dimer adopts conventional folding (Fig. 1b), each containing an $InsP_6$-sensing SPX domain and features ten transmembrane helices (TM1–TM10), an intracellular amphipathic helix (AH), and a cytosolic C-loop (Fig. 1b, d). The transmembrane core consistently segregated into two functional modules, as established in prior studies: the N-domain (TM1–TM4), mediating dimerization, and the EXS domain (TM5–TM10), constituting the phosphate transport channel.

Earlier structural studies of isolated XPR1 observed the SPX domain in higher-order InsP-bound states ($InsP_7$ or $InsP_8$)[28,29,34] (Supplementary Fig. 5a,b), but failed to resolve it under $InsP_6$-presence conditions[26,27,29,30,34] (Supplementary Fig. 6). Strikingly, our analysis of the XPR1–KIDINS220$^{1-722}$ complex revealed clear density, enabling the unambiguous modeling of the SPX domain fold and orientation in the presence of $InsP_6$ (Fig. 1b, Supplementary Fig. 3b). Compared to the isolated $InsP_7$-bound XPR1 structure[29], the SPX dimer in our complex retains its position beneath the transmembrane domain (TMD) but adopts a distinct, ~ 180°-rotated conformation (Supplementary Fig. 5c). In isolated XPR1^{InsP7}, the SPX dimer binds four $InsP_7$ molecules (Supplementary Fig. 5d,e): two ($InsP_7$-1/2) stabilize the dimer interface via the canonical positively charged surface (formed by clustered N- and C-terminal basic residues across subunits), while two others ($InsP_7$-3/4) bind individual SPX C-termini. Critically, these C-terminal-bound $InsP_7$ molecules bridge to basic residues surrounding the tip of the intracellular amphipathic helix in the TMD (Supplementary Fig. 5e), thereby coupling SPX-TMD interactions. In our complex, the rotated SPX dimer exhibits no density at the central dimer interface (occupied by $InsP_7$-1/2 in isolated XPR1). Instead, extra density localizes to the N-terminal basic surface of each SPX monomer,

which we interpret as two $InsP_6$ molecules ($InsP_6$-A/B) (Supplementary Fig. 5f,g). Notably, these $InsP_6$ sites spatially overlap with $InsP_7$-3/4 positions (Supplementary Fig. 5h), suggesting analogous $InsP_6$-mediated SPX-TMD tethering (Fig. 1e).

In our $XPR1^{InsP6}$ structure, although the cryo-EM map clearly resolved the backbone architecture surrounding the $InsP_6$-binding sites, the side-chain densities of several coordinating basic residues were insufficient to unambiguously define the underlying electrostatic interaction network (Fig. 1e). To characterize the binding interface at atomic resolution, we performed all-atom molecular dynamics (MD) simulations for the $XPR1^{InsP6}$ structure (Supplementary Fig. 7a). Four independent 1-μs simulations revealed consistent and stable XPR1-$InsP_6$ interactions (Supplementary Fig. 7b). The most frequently engaged residues include a cluster of N-terminal basic residues (K26, K158, K161, K162, K165) and the TMD-located residues (R308, K364, K369) (Fig. 1f). Importantly, these MD-derived high-occupancy contacts closely recapitulated the $InsP_6$-binding pocket observed in our cryo-EM structure (Fig. 1e). To functionally validate these electrostatic contacts, we mutated key TMD basic residues (including R308, K364, K369) to alanine, and measured $InsP_6$ binding affinity to the XPR1–$KIDINS220^{1-722}$ complex (Fig. 1g). The results showed that these substitutions resulted in reduced $InsP_6$ binding (Fig. 1g), corroborating the structural model. Together, these observations suggest that KIDINS220 association facilitates SPX domain stabilization by enabling $InsP_6$ to form electrostatic interdomain links, uncovering an allosteric mechanism not previously observed in isolated XPR1 structures.

Previous cryo-EM analysis revealed conformational heterogeneity in TM9b—the gating element of the Pi channel—within dimeric XPR1 under $InsP_6$-bound conditions[26,27,29,30,34], sampling symmetric closed-closed, symmetric open-open, and asymmetric open-closed states (Supplementary Fig. 6). Strikingly, upon association with $KIDINS220^{1-722}$, our $InsP_6$-bound XPR1 structure adopts a uniform TM9b-closed conformation across all protomers (Fig. 1h). These data indicate that KIDINS220 exerts dual regulatory effects: (i) stabilizing the SPX domain via assembly of $InsP_6$-bridged SPX-TMD interface, and (ii) allosterically trapping the transporter in a channel-closed state. This conformational constraint suggests impaired phosphate transport activity—a functional consequence explored in subsequent sections.

Live-cell FLIM-FRET characterizes KIDINS220-driven N–C terminal compaction of XPR1

Our cryo-EM structure demonstrates that KIDINS220 binding stabilizes the SPX domain and induces an ~180° rotational shift relative to isolated XPR1 conformations (Supplementary Fig. 5c). This shift repositions the SPX N terminus toward the XPR1 C-terminal region (Fig. 2a). To probe this conformational modulation in living cells, we employed Förster resonance energy transfer combined with fluorescence lifetime imaging microscopy (FLIM-FRET) analysis. We engineered an FLIM-FRET reporter by fusing mTurquoise2 (donor) to the XPR1 C terminus and SYFP2 (acceptor) to the N terminus (Fig. 2b), enabling detection of N–C terminal proximity via changes in donor fluorescence lifetime (τ_D). The C-

terminal donor construct (XPR1^{Donor}) showed robust fluorescence localized to the cell membrane (Supplementary Fig. 8a, line 1). However, additional N-terminal SYFP2 fusion resulted in severely diminished fluorescence intensity (Supplementary Fig. 8a, line 2), suggesting impaired expression. To resolve this, we introduced flexible linkers between SYFP2 and XPR1. Constructs incorporating 9- or 12-residue linkers restored fluorescence and proper membrane localization (Supplementary Fig. 8a, lines 3–4). Notably, the 9-residue linker (GGSGGSGGS) yielded the maximal donor lifetime shift (Supplementary Fig. 8b), indicating superior detection sensitivity. We therefore utilized this optimized reporter (XPR1^{FRET}) for all subsequent analyses.

In mammalian cells, both the XPR1^{Donor} and XPR1^{FRET} constructs exhibited stable fluorescence (Fig. 2e). Quantitative FLIM analysis revealed that the average donor lifetime decreased from ~ 4.2 ns in XPR1^{Donor} to ~ 3.5 ns in XPR1^{FRET} (Fig. 2e,g). This reduction confirms efficient FRET, validating the reporter as a sensitive probe for monitoring N–C terminal proximity and conformational changes in live cells.

We then co-expressed XPR1^{FRET} with KIDINS220 (residues 1-722), which carried a C-terminal sfGFP tag (Fig. 2b). Clear fluorescent signals indicated proteins expression and membrane colocalization (Fig. 2f, line 1). The presence of KIDINS220 markedly decreased the average donor lifetime from ~ 3.5 ns to ~ 2.8 ns (Fig. 2f,g), suggesting that KIDINS220 induces N–C terminal proximity in XPR1. Furthermore, lifetime distribution analysis revealed a shifted peak towards shorter lifetimes and a narrowed half-width in the KIDINS220 co-expression group (Fig. 2h,i), indicating that KIDINS220 promotes a more compact and conformationally homogeneous population of XPR1. This effect was independently validated using N-terminally mCherry-tagged KIDINS220, which similarly shortened donor lifetime (Supplementary Fig. 8c,d). These cellular FRET data corroborate our structural observations of SPX domain reorientation, demonstrating that KIDINS220 enhances XPR1 conformational stability by constraining the relative orientation of the SPX domain and the C-region.

To define the structural basis of KIDINS220-induced conformational modulation, we mapped the XPR1-KIDINS220 interface through integrated computational and biochemical approaches. Although unresolved in our cryo-EM structure, AlphaFold3 modeling predicted[40] that the KIDINS220 AR domain engages the XPR1 C-terminal helix (corresponding to residues 633–668) (Supplementary Fig. 9a). Pull-down assays confirmed this topology: KIDINS220$^{1-722}$ (containing AR and TMD domains) and KIDINS220$^{1-489}$ (AR-only) retained XPR1 binding, whereas KIDINS220$^{489-765}$ (TMD-only) showed no interaction (Supplementary Fig. 9b,c). Conversely, deletion of the XPR1 C-terminal helix (XPR1$^{1-632}$, lacking residues 633–696) completely abrogated binding, whereas full-length XPR1 and the C-terminal helix-containing construct (XPR1$^{1-668}$), maintained robust interaction (Supplementary Fig. 9b,c). These data establish a direct AR domain–C-helix interface as the structural determinant of complex formation, enabling KIDINS220-mediated conformational stabilization of XPR1.

Guided by the predicted AR domain–C-helix interface (Fig. 2c, Supplementary Fig. 9a), we designed a charge-reversal mutant (KIDINS220^{Mut}: K168E/R179E/K180E) targeting key electropositive residues

within the binding surface of the AR domain (Fig. 2c). Pull-down assays revealed near-complete loss of XPR1 binding (Fig. 2d). Consistent with this, cellular co-expression of KIDINS220^{Mut} with XPR1^{FRET} yielded a mean donor lifetime (3.60 ± 0.05 ns) similar to that of XPR1^{FRET} alone (3.50 ± 0.04 ns) (Fig. 2e-g). Lifetime distributions analysis further confirmed the absence of a conformational shift (Fig. 2h,i). These results demonstrate that the FRET lifetime decrease requires a direct KIDINS220–XPR1 interaction, supporting a model in which KIDINS220 stabilizes an N–C-proximal conformation of XPR1 in cells.

Conformations of KIDINS220-associated XPR1 in sensing InsP and phosphate

Upon interaction with KIDINS220, our $InsP_6$-bound structure of XPR1 was determined in a channel-closed state, characterized by the full occlusion of TM9b (Fig. 1h). To gain further insights into the transport mechanism of XPR1 in the presence of KIDINS220, we introduced inorganic phosphate (Pi) during sample preparation to capture a transport-relevant conformation of the XPR1–KIDINS220$^{1–722}$ complex. This approach yielded a 3.6-Å cryo-EM reconstruction (designated XPR1$^{InsP6•Pi}$) with both $InsP_6$ and Pi were present (Supplementary Figs. 10a-g, Supplementary Table 1). In this structure, the TMD and SPX domains of the XPR1 dimer exhibit well-defined density (Fig. 3a,b, and Supplementary Fig. 11), whereas the presumably density of KIDINS220 is weak (Fig. 3c), similarly to that observed in XPR1^{InsP6}, it displayed pronounced conformational heterogeneity, appearing as fragmented densities that precluded structure modeling (Supplementary Fig. 4b).

Comparison with the closed-state XPR1^{InsP6} structure revealed conformational changes in the XPR1$^{InsP6•Pi}$ complex. The SPX domain underwent lateral deflection toward one side of the TMD dimer and was repositioned beneath the membrane plane (Fig. 3b, Supplementary Fig. 12a). This repositioning generated two distinct electropositive interfacial clefts: an SPX-SPX dimeric interface and an SPX-TMD contact zone (Supplementary Fig. 12b). These clefts contain unassigned density that presumably accommodates two $InsP_6$ molecules, though the poor resolvability of surrounding side-chains precludes atomic modeling (Supplementary Fig. 12c). Consequently, the bound $InsP_6$ molecules primarily indicate KIDINS220-mediated conformational stabilization, whereby KIDINS220 enforces this reoriented architecture—simultaneously engaging both interfacial regions—to restrict SPX mobility and and maintain conformational stability during phosphate sensing.

In the KIDNIS220-associated XPR1$^{InsP6•Pi}$ complex structure, while the initial reconstruction resolved the SPX domain, the transmembrane domain (TMD) remained poorly defined, precluding a precise assessment of the TM9b conformation. Motivated by this limitation, we performed local 3D classification using a mask encompassing the TMD region, followed by local refinement, yielding a 3.6-Å membrane-specific map (designated XPR1^{TMD}) with interpretable density for the TMD (Fig. 3d, Supplementary Fig. 10h-k). This refined map revealed that the protomer adopts an open-like

arrangement of TM9b (Fig. 3e, Fig. 4a). Additionally, sequential focused 3D classification on the TMD of each protomer within the dimer resolved three recurrent TM9b configurations: a both-open state, a both-closed state, and an asymmetric open-closed state (Supplementary Figs. 10h,l and 13). This conformational heterogeneity indicates dynamic sampling of TM9b states and suggests structural independence between protomers during gating.

The XPR1^{TMD} cryo-EM map additionally revealed non-protein densities within the transmembrane channel. These channel-lining densities (Fig. 3f), modeled as phosphate ions, occupy positions congruent with phosphate-binding sites in previously determined isolated XPR1 structures[27] (Supplementary Fig. 14). This spatial conservation reinforces the channel-like transport mechanism and demonstrates invariance of the core translocation pathway across distinct functional states—from monomeric XPR1 assemblies to KIDINS220-bound complexes.

KIDINS220-mediated inhibition of XPR1 transport

It is established that full functionality of XPR1 requires TM9b opening to allow Pi ion passage, concurrent with the displacement of the C-plug from the transmembrane channel entrance to facilitate Pi accessibility[27,28,34]. In the KIDINS220-bound XPR1$^{InsP6•Pi}$ complex, we captured a conformation featuring TM9b opening, consistent with a state poised for Pi translocation (Fig. 4a). To further elucidate how KIDINS220 modulates XPR1, we analyzed the KIDINS220-associated XPR1$^{InsP6•Pi}$ structure with a focus on the cytoplasmic C-plug region.

In the KIDINS220-associated XPR1$^{InsP6•Pi}$ structure, the C-plug is tightly lodged at the entrance of the cytoplasmic cavity, effectively occluding the substrate translocation pathway (Fig. 4a). Notably, this occluded configuration contrasts sharply with the released C-plug state observed in previously reported structures of $InsP_6$- and Pi-bound isolated XPR1[27] (Fig. 4b). In the XPR1$^{InsP6•Pi}$ structure, the C-plug residue F623 engages in hydrophobic interactions with TM5 residues F391 and F394, forming a compact aromatic network. Concurrently, C-plug residues E622 and R624 likely establish electrostatic contacts with R466 on TM6 and with N614 and E615 on TM10 (Fig. 4c). These cooperative interactions synergistically lock the C-plug in its occluded position. These observations indicate that KIDINS220 modulates the C-plug in a plugged conformation, restricting phosphate access to the translocation pathway, which may lead to impaired phosphate transport.

To functionally validate the structural observations of KIDINS220-induced XPR1 inhibition, we performed phosphate transport assays using a reconstituted proteoliposome system. Purified and preformed XPR1–KIDINS220$^{1-722}$ complex was reconstituted into liposomes, and phosphate uptake was quantified via [^{32}P]-Pi radiotracer assays. Our previous report demonstrated that proteoliposomes containing XPR1 alone exhibited robust Pi uptake upon external phosphate addition (Fig. 4d)[26]. Strikingly, co-reconstitution with KIDINS220$^{1-722}$ significantly reduced XPR1-mediated phosphate transport (Fig. 4d). These functional data confirm that KIDINS220 binding suppresses XPR1 transport activity,

mechanistically consistent with its structural role in stabilizing the C-plug occlusion and preventing conformational transitions required for Pi translocation.

Discussion

In this study, we determined cryo–EM structures of the KIDINS220$^{1-722}$-associated XPR1 under distinct conditions, demonstrating that KIDINS220 modulates the conformational landscape of XPR1. In the $InsP_6$-bound state, KIDINS220 anchors the SPX domain, stabilizing the transporter in a channel-closed conformation. Upon further sensing Pi under $InsP_6$ conditions, the SPX domain deflects toward one side of the TMD, and TM9b shifts to an open conformation—consistent with substrate translocation—yet the C-plug remains occluded at the cytoplasmic entrance, obstructing Pi access. This trapped TM9b-open/C-plug-occluded intermediate represents a novel transport-inhibited state. These findings demonstrate that KIDINS220 effectively restricts XPR1 in a non-active state by stabilizing either the SPX domain or the C-plug—a mechanistic interpretation functionally validated by phosphate transport assays.

A very recent cryo-EM study of the KIDINS220$^{1-1072}$-associated XPR1 described InsP-induced SPX rearrangements primarily based on map-level features[28]. Here, our reconstruction demonstrates a well-defined SPX conformation, allowing molecule-level interpretation. This XPR1^{InsP6} conformation aligns with structural data from another recently reported KIDINS220-associated XPR1 structure, which included a different KIDINS220 fragment (KIDINS220$^{1-432}$, containing only the AR domain)[41] (Supplementary Fig. 15a), mutually corroborating KIDINS220's modulation of XPR1. Upon Pi sensing under $InsP_6$ conditions, we observe TM9b opening—consistent with prior findings[41] (Supplementary Fig. 15b)—but additionally identify a novel SPX lateral deflection (Supplementary Fig. 15c). This rearrangement reveals a distinct regulatory architecture wherein KIDINS220 reshapes XPR1's ligand-sensing interface. These findings highlight the SPX domain as a versatile regulatory hub that adopts context-dependent configurations—stabilized by partner proteins and ligands—to gate XPR1 between inhibited and activation-permissive states.

Prior work established that KIDINS220 knockout reduces XPR1-dependent phosphate export, indicating its essential role in promoting XPR1 function, as it facilitates proper trafficking and cell-surface localization of the transporter[16]. Our data here further reveal a dual regulatory paradigm: Upon reaching the plasma membrane, KIDINS220 physically engages XPR1 to impose direct inhibitory constraints on its transport activity. Thus, KIDINS220 serves as both a trafficking chaperone and a membrane-localized brake on XPR1 function. We propose this bipartite regulation establishes an activation threshold for phosphate export, positioning KIDINS220 as a molecular safety valve that prevents excessive phosphate efflux during metabolic stress or signaling imbalance.

Integrating these structural and functional insights, we propose a cooperative gating model wherein $InsP_6$ binding primes the KIDINS220-associated XPR1 for Pi-responsive activation (Fig. 4e). In this model, XPR1 maintains an inhibited state under $InsP_6$-only condition, while $InsP_6$ and Pi co-occupancy

induces a transport-intermediate conformation—characterized by partial TM9b opening with persistent C-plug occlusion. This establishes Pi as a dual-function molecule: it serves as both the exported substrate and an allosteric trigger that licenses conformational progression beyond the KIDINS220-imposed inhibition threshold. This mechanism enforces demand-driven phosphate export, requiring sufficiently high intracellular Pi levels to overcome the cooperative activation barrier and permit channel opening.

Collectively, this tiered regulatory architecture—integrating KIDINS220 scaffolding, $InsP_6$ sensing, and Pi allostery—reveals unprecedented complexity in XPR1 governance and underscores the need for future work to resolve the precise dynamics governing phosphate export. We propose this multivalent control system enables precise calibration of transporter activity, functioning as a fail-safe mechanism that prevents dysregulated phosphate efflux during metabolic perturbations while maintaining stringent phosphate homeostasis.

Methods

Protein expression and purification

Full-length Human *XPR1* (Uniprot ID: Q9UBH6) gene was subcloned into a pMlink vector with a 3×Flag affinity tag at C-terminus. And human *KIDINS220* (Uniprot ID: Q9ULH0) as 1-722 fragment gene was subcloned into a pMlink vector with a 2×Strep affinity tag and sfGFP at N-terminus. All site-specific mutations were introduced by the Fusion PCR method and verified by DNA sequencing.

Recombinant plasmids of XPR1 and KIDINS220 were co-transfected in Expi293F mammalian cells (Invitrogen) via transient transfection. Cells were cultured in Union-293 media (Union-Biotech, Shanghai) and were transfected at a density of 2.0×10^6 cells per milliliter. The plasmids were transfected in cells with 4 kDa linear polyethylenimine (PEI) (Polysciences). Transfected Cells were cultured at 37°C under 5% CO_2 for 60 hours before harvesting. To prepare the cryo-EM sample, the transfected cells were collected by centrifugation at 2000 rpm for 20 minutes.

For purification of the $XPR1^{InsP6}$ sample, the pellets were resuspended in buffer A containing 100 mM Tris-HCl (pH 8.0), 150 mM NaCl, 1.0% (w/v) LMNG (Anatrace), 0.1% (w/v) CHS (Anatrace), 0.25% (w/v) SoyPhospholipids (Sigma) and 1 mM $InsP_6$ (a commercially available surrogate for PP-InsPs)[26,42]. After incubation at 4°C for 1.5 hours, the supernatant was isolated by centrifugation at 20,000×g for 50 minutes and incubated with Strep-Tactin XT 4Flow resin (IBA) at 4°C for 1 h, then the resin was rinsed with 30 bed volumes of buffer B containing 100 mM Tris-HCl (pH 8.0), 150 mM NaCl, 0.06% digitonion (Anatrace) and 1 mM $InsP_6$, followed elution with wash buffer containing 50 mM D-Biotin (BBI).The elute proteins was concentrated and incubated with anti-Flag G1 affinity resin (Genscript) at 4°C for 1 hours. The bound target proteins were washed with 30 bed volumes of buffer C containing 50 mM Tris-HCl (pH 7.4), 150 mM NaCl, 0.06% digitonion (Anatrace), and 1 mM $InsP_6$, followed elution with buffer B containing 0.25 mg/mL Flag peptide (Genscript). The sfGFP and 2×Strep affinity tag was cleaved by TEV

protease (1:25 w/w ratio) on ice for 2 h. Then the eluent was concentrated and applied to size-exclusion chromatography (SEC) using a Superose-6 Increase 10/300 column (GE Healthcare) in Buffer D containing 25 mM Tris-HCl (pH 8.0), 150 mM NaCl, 2 mM DTT, 1 mM $InsP_6$, and 0.06% digitonion (Anatrace). The peak fractions of target proteins were pooled and concentrated to 6.5 mg/mL for cryo-EM grid preparation.

For purification of the $XPR1^{InsP6•Pi}$ and $XPR1^{TMD}$ sample, the pellets were resuspended in buffer E containing 20 mM HEPES (pH 7.5), 150 mM NaCl, 1 mM $InsP_6$, 2 mM DTT, 1 mM PMSF, 1% (w/v) n-dodecyl-β-D-maltoside (Anatrace) and 0.15% (w/v) CHS. After incubation at 4°C for 1.5 h, the supernatant was isolated by centrifugation at 20,000×g for 50 minutes and incubated with Strep-Tactin XT 4Flow resin (IBA) at 4°C for 1 h, then the resin was rinsed with 10 bed volumes of buffer F containing 20 mM HEPES (pH 7.5), 150 mM NaCl, 1 mM $InsP_6$, 2 mM DTT, and 0.06% (w/v) GDN (Anatrace), followed elution with buffer F containing 50 mM D-Biotin (BBI). The elute proteins was concentrated and incubated with anti-Flag G1 affinity resin (Genscript) at 4°C for 40 min. The bound target proteins were washed with 30 bed volumes of buffer F and followed elution with buffer F containing 0.25 mg/mL Flag peptide (Genscript). The sfGFP and 2×Strep affinity tag was cleaved by TEV protease (1:25 w/w ratio) on ice for 1 h. Then the eluent was concentrated and applied to size-exclusion chromatography (SEC) using a Superose-6 Increase 10/300 column (GE Healthcare) in Buffer G containing 25 mM NaH_2PO_4 (pH 7.5), 150 mM NaCl, 2 mM DTT, and 0.0075% (w/v) GDN (Anatrace). The peak fractions of target proteins were pooled and concentrated to 8.5 mg/mL for cryo-EM grid preparation.

Samples used for the proteoliposome-based transport assays were extracted from transfected cells using buffer I containing 50 mM Tris-HCl (pH 7.4), 150 mM NaCl, and 1% (w/v) n-dodecyl-β-D-maltoside (Anatrace). The proteins were purified using anti-Flag G1 affinity resin, Strep-Tactin XT 4Flow resin, and followed by a Superose-6 Increase 10/300 column. The purified proteins were then prepared in a buffer containing 25 mM Tris-HCl (pH 7.4), 150 mM NaCl, 2 mM DTT, and 0.02% n-dodecyl-β-D-maltoside (Anatrace) for proteoliposome reconstitution.

Cryo-EM grid preparation and data acquisition

Holey carbon grids (Quantifoil Cu R1.2/1.3, 300 mesh) were glow discharged (PELCO easiGlow) at 15 mA for 40 s. 3.5 μL aliquots of the purified protein were dispensed onto grids. The grids were blotted with a Vitrobot Mark IV (ThemoFisher Scientific) using 3.5 s blotting time with 100% humidity and 8°C, and were plunge-frozen in liquid ethane cooled by liquid nitrogen.

Cryo-EM data were collected on a Thermo Scientific Krios G4 transmission electron microscope operating at 300 kV, equipped with a Falcon 4 direct electron detector positioned post a Thermo Scientific Selectris energy filter (slit width 10 eV). E Pluribus Unum (EPU) software was used for fully automated data collection. For the $XPR1^{InsP6}$ dataset, data were collected at a nominal magnification of 130,000×, corresponding to a pixel size of 0.93 Å. For the $XPR1^{InsP6•Pi}$/$XPR1^{TMD}$ datasets, data were

collected at a nominal magnification of 165,000×, resulting in a pixel size of 0.73 Å. All image stacks composed of 42 movie frames were collected with a preset defocus range from − 0.8 to -2.2 µm and a dose rate of 5.0 e-/pixel/s, resulting in a total electron dose of 50 e-/Å.

Cryo-EM data processing

Data processing workflows are summarized in Supplementary Figs. 2 and 10. All movie stacks were processed using CryoSPARC (v4.6.0)[43]. Motion correction was performed using the Patch Motion implementation, and contrast transfer function (CTF) parameters were estimated via Patch CTF estimation.

For the XPR1^{InsP6} dataset (Supplementary Fig. 2), 9,931 movies were imported and processed. A total of 6,359,431 particles were auto-picked and subjected to iterative 2D classification to discard junk particles, resulting in a selected subset of 2,558,620 particles. These particles underwent ab initio reconstruction and heterogeneous refinement to isolate classes exhibiting clear membrane protein features. Particles from the dominant class were further processed by heterogeneous refinement and non-uniform (NU) refinement, yielding a consensus reconstruction at 3.6 Å.

Inspection of this map at a low threshold (0.035) revealed an additional weak density tentatively attributed to KIDINS220, suggesting significant conformational heterogeneity or partial occupancy. To investigate this region, a focused mask encompassing the putative KIDINS220 density was generated for focused 3D classification. The resulting classes confirmed the pronounced heterogeneity of this density, which precluded high-resolution refinement of the region.

Consequently, we prioritized the quality of the core complex. Seed-facilitated 3D classification[44] was performed to enrich for high-quality particles, yielding a subset of 343,343 particles that reached 3.2 Å after NU refinement. To further resolve the SPX domain, a focused 3D classification was applied using an SPX-specific mask. A subclass showing improved signal-to-noise in the SPX region was selected and subjected to final rounds of heterogeneous and NU refinement, resulting in a final reconstruction at 3.6 Å (designated XPR1^{InsP6}).

For the XPR1$^{InsP6•Pi}$/XPR1^{TMD} dataset (Supplementary Fig. 10), 13,550 movies were processed as described above. A total of 8,205,750 particles were auto-picked, and 3,447,385 particles were selected following multiple rounds of 2D classification. These particles were subjected to ab initio reconstruction and heterogeneous refinement. Classes displaying well-defined micelle density were selected for further heterogeneous and NU refinement, yielding a reconstruction at 3.3 Å.

Similar to the XPR1^{InsP6} dataset, an additional weak density corresponding to KIDINS220 was discernible only at a very low threshold (0.027). Focused 3D classification targeting this region confirmed its highly dynamic nature, preventing reliable high-resolution reconstruction. We therefore shifted our strategy to improve the SPX regions. Focused 3D classification was performed using masks targeting the SPX

domain. Processing with the SPX-focused mask, followed by heterogeneous and NU refinement, produced a map with improved SPX resolvability at 3.6 Å (designated $XPR1^{InsP6•Pi}$).

To enrich for well-resolved particles prior to downstream analysis, seed-facilitated 3D classification was performed, yielding 973,307 particles and a global reconstruction at 3.4 Å. To resolve conformational heterogeneity in the TM9 region, a focused 3D classification was performed using a mask centered on TMD of the SPX-proximal monomer, which separated particles into open and closed conformations. Particles from these branches were subsequently classified using a TM9 mask on the opposing monomer, revealing open/closed states for the second subunit. The final classes, corresponding to both TM9 helices in the open state and both in the closed state, were subjected to local refinement, yielding reconstructions at 3.6 Å (open/open), (designated $XPR1^{TMD}$) and 4.1 Å (closed/closed), respectively.

For all reconstructions, resolution estimates were determined based on the gold-standard Fourier shell correlation (FSC)[45] 0.143 criterion. Local resolution maps were estimated in cryoSPARC.

Model building and refinement

The initial model of XPR1 was predicted from the AlphaFold2[46]. Models for all structures were constructed by rigid-body fitting of individual domains into the corresponding maps using the initial model, followed by iterative rounds of coordinate adjustment and local refinement in Coot[47]. Model refinement was performed using PHENIX[48] with secondary structure and geometry restraints. Model quality was assessed using MolProbity scores[49], Ramachandran plots, and EMRinger[50]. Structural figures were prepared using UCSF ChimeraX (v1.6.1) and Pymol (v2.4.1).

Molecular dynamic (MD) simulations

An atomistic model of the $InsP_6$-bound XPR1 dimeric complex ($XPR1^{InsP6}$) was constructed based on the corresponding cryo-EM structure. Missing loop regions were modeled using AlphaFold3 predictions as structural templates. KIDINS220 was not included in the system. The resulting $XPR1^{InsP6}$ model was then embedded in a POPC lipid bilayer and solvated in a cubic water box containing 0.15 M NaCl. The dimensions of the box were 14.1 nm x 14.1 nm x 10.6 nm in the x, y, and z directions, respectively, totaling approximately 220,000 atoms. The transmembrane region was aligned in the lipid bilayer using the OPM (Orientations of Proteins in Membranes) webserver. Construction of the system was facilitated by the CHARMM-GUI webserver[51], followed by energy minimization using the steepest descent algorithm and a six-step equilibration process with gradual removal of position constraints. Production runs under semi-isothermal-isobaric (NPT) conditions were conducted using the CHARMM36m force field[52] for proteins and lipids, along with the TIP3P model for water. The $InsP_6$ molecules were parameterized using the CHARMM General Force Field (CGenFF)[53]. During the MD simulations, temperature was maintained at 310 K with a Nosé–Hoover thermostat and a coupling constant of 1 ps, and pressure was kept at 1.0

bar using the Parrinello–Rahman barostat and a time coupling constant of 5 ps. A switch function with a starting distance of 1.0 nm was employed for a van der Waals cut-off of 1.2 nm. Short-range electrostatic interactions were also truncated at 1.2 nm, while long-range electrostatic interactions were computed via the particle mesh Ewald decomposition algorithm with a 0.12-nm mesh spacing. The hydrogen mass repartitioning technique[54] was used, allowing simulations to be performed with an integration time step of 2.5 fs. For each system, four independent 1000 ns MD simulations were conducted using the GPU-accelerated version of Gromacs 2026.1[55]. Trajectory analysis was performed using Gromacs gmx tools and custom scripts.

Microscale thermophoresis measurement

The $InsP_6$ binding affinity of KIDINS220$^{1-722}$-associated XPR1 and its mutants were measured by microscale thermophoresis using a Monolith NT.115 instrument (Nano Temper Techologies, Germany). Proteins were prepared through size exclusion chromatography in a SEC buffer containing 25 mM Tris pH 8.0, 150 mM NaCl and 0.02% GDN. The protein was labeled by mixing it with FITC (Fluorescein-5-Maleimide) dye at a molar ratio of 1:10. After 1 h incubation at room temperature, the excess dye was removed by using a desalting column. A volume of 10 μL of 75 ~ 100 nM dye-labeled KIDINS220$^{1-722}$-associated XPR1 was mixed with 10 μL ligand (varying concentrations between 61.04 nM and 0.5 mM) in the SEC buffer. The complex-ligand mixture was loaded into capillaries (Nano Temper Technologies), and thermophoresis was measured at 25°C with an excitation power of 20% and an MST power of medium. Data from at least three independent measurements were combined and analyzed using MO Affinity Analysis software (Nano Temper Technologies), and fitted to a single binding site model.

Co-immunoprecipitation analysis

To investigate the interaction mode between KIDINS220 and XPR1, recombinant plasmids of XPR1 and KIDINS220 were co-transfected in Expi293F mammalian cells (Invitrogen) by transient transfection using 4-kDa linear polyethylenimine (PEI; Polysciences). Transfected cells were cultured at 37°C under 5% CO_2 for 60 hours before harvesting. The cells were centrifuged and washed once with 1× PBS buffer and then lysed with the lysis buffer (25 mM Tris-HCl at pH 8.0, 150 mM NaCl, 1% (w/v) n-dodecyl-β-D-maltoside (DDM) and 1 mM PMSF). Cell suspensions were briefly sonicated and further incubated on ice for 10 min. Lysates were clarified by centrifugation at 14,000 rpm for 20 min at 4°C. The protein contents were quantified by bicinchoninic acid analysis. 50 μg of proteins were taken as input samples and mixed with 2× loading buffer. Equal amounts of the residual proteins were incubated with Flag beads at 4°C for 1 h under slow rotation. The beads were washed by the wash buffer (25 mM Tris-HCl at pH 8.0, 150 mM NaCl, 0.02% DDM). Subsequently, the proteins were eluted with the elution buffer (25 mM Tris-HCl at pH 8.0, 150 mM NaCl, 1% DDM and 0.25 mg/mL Flag pepetide) at ice for 30 min. The elution was separated and combined with a 5× loading buffer to prepare co-IP samples. The input samples and co-IP samples (without boiling) were separated on 12% polyacrylamide gels and then transferred to PVDF membranes

under constant current conditions. The PVDF membranes were cut according to molecular weight and then incubated overnight at 4°C with the indicated primary antibodies, respectively. The following primary antibodies were utilized in this study: Anti-flag Tag Mouse Monoclonal Antibody (Proteintech, diluted 1:3000), Anti-strep Tag Mouse Monoclonal Antibody (Abbkine, diluted 1:3000) and GAPDH antibody (Proteintech, diluted 1:3000). Subsequently, the membranes were washed three times in 1× PBST buffer and further incubated with Goat anti-Mouse IgG secondary antibody (Proteintech, diluted 1:10000) at room temperature for 40 min. After incubation, the membranes were washed for 15 minutes with PBST and treated with SuperKine ECL (Abbkine) for 1 to 5 minutes. The blots were detected using chemiluminescence imaging system (Fusion, VILBER).

Proteoliposome-based transport assay

The Pi transport assay was conducted according to established methods[26]. For reconstitution of proteoliposomes, *E. coli* total extract (Avanti Polar Lipids) was resuspended in 10 mM HEPES-Tris (pH 7.5), and 100 mM KCl to a final concentration of 10 mg/mL. Preformed liposomes were solubilized with 1.3% (w/v) DDM by sonication until clear. Then the proteins were mixed with liposomes at a protein-to-lipid ratio of 1:100 (w/w) and incubated at 4°C for 1.5 h. DDM was removed by adding SM-2 bio-beads (Bio-Rad) at a DDM-to-bio-bead ratio of 1:20 (w/w) and incubating overnight. Prior to the start of the transport assay, the proteoliposomes were extruded through a 200 nm polycarbonate filter (Whatman) to homogeneity.

15 µL of proteoliposomes containing 0.2–0.5 µg of protein were diluted into 80 µL of reconstitution buffer. Pi transport reactions were initiated by adding a KPi mixture at the indicated concentration, consisting of non-labeled KH_2PO_4 and [^{32}P] KH_2PO_4 (3.7 MBq/µmol; PerkinElmer) in a molar ratio of 20:1. Reactions were carried out at 37°C and terminated at defined time points by a tenfold dilution with ice-cold stop buffer (10 mM HEPES-Tris, pH 7.4, 100 mM KCl and 5 mM non-labeled KH_2PO_4), followed by rapid filtration through nitrocellulose membrane (Millipore, 0.22 µm Triton-free MCE). The filters were subsequently washed with 10 mL of ice-cold stop buffer, placed in 5 mL Optiphase HiSafe 3 scintillation fluid and counted after 14 h. Background counts were determined from parallel transport assays that were terminated immediately upon initiation. After background subtraction, the amount of phosphate transported into the proteoliposomes was quantified by comparison to a standard curve of [^{32}P] KH_2PO_4. The standard curve was established by diluting [^{32}P] KH_2PO_4 in water and measuring the corresponding radioactivity, thereby providing a quantitative relationship between counts per minute (cpm) and the amount of [^{32}P]-labeled phosphate. This relationship was used to calculate the amount of Pi taken up during our transport assays. The protein content in the proteoliposomes was assessed by SDS–PAGE and quantified using ImageJ. The phosphate uptake was expressed as pmol Pi per µg of protein. Each data point was independently performed a minimum of three times, with results presented as mean ± standard deviation (SD).

Fluorescence lifetime imaging and FLIM-FRET analysis

Hela cells were cultured in Dulbecco's modified Eagle's medium (DMEM, Gibco) supplemented with 10% fetal bovine serum (FBS) and 1% penicillin-streptomycin mixture in a 5% CO2 incubator at 37°C. The cell line was subjected to mycoplasma testing once per month and found to be negative. For Fluorescence lifetime imaging and FLIM-FRET analysis, all constructs were transfected using the Polyethylenimine Linear (PEI) MW40000 transfection reagent (40816ES02, Yeasen) under the conditions specified by the manufacturer.

FLIM-FRET measurements were carried out according to established methods[56], using the Q2 time-resolved confocal imaging system (ISS Inc., Champaign, Illinois, USA). It is coupled to a Nikon Ti2U microscope equipped with a Nikon 60×/1.2NA water objective lens. The 440 nm pulsed diode laser at the 20-MHz repetition rate was used as the excitation source for the FRET donor. The donor emission light was detected by a single photon counting avalanche photodiode detector (Excelitas SPCM-AQRH-45) using the 475/35-nm bandpass filter. For each experimental condition, images were acquired using the one-airy-unit pinhole size (50 μm), with a frame size of 256 × 256 pixels and a pixel dwell time of 0.4 ms to ensure optimal image quality and resolution. To determine the phase delays (φ) and modulation ratios (m) of the fluorescence signal in response to the excitation, we calibrated the instrument response function (IRF) using the Alexa Fluor 488 standard solution with a known fluorescence lifetime of 4 ns. The fluorescence lifetime of the FRET donor was determined for each pixel by the mono-exponential decay fitting of the frequency-domain data (phase delays & modulation ratios) in the VistaVision software (ISS Inc., USA).

The full-width-at-half-maximum (FWHM) was calculated using a custom-written MATLAB (MathWorks) script, within the analysis window, the global maximum of the response $\mathrm{y}(\mathrm{x})$is taken as the peak height $\mathrm{y}_{\mathrm{peak}}$, and the half-height is defined as $\mathrm{y}_{\mathrm{half}}=\mathrm{y}_{\mathrm{peak}}/2$. On either side of the peak, adjacent sample points satisfying $\mathrm{y}(\mathrm{x})\leq\mathrm{y}_{\mathrm{half}}$ are identified, and linear interpolation is used to compute the left and right intersections $\mathrm{x}_1$and $\mathrm{x}_2$with the line $\mathrm{y}=\mathrm{y}_{\mathrm{half}}$. The FWHM is then defined as $\mathrm{FWHM}=|\mathrm{x}_2\text{-}\mathrm{x}_1|$. All statistical analyses were performed using GraphPad Prism 9 Software (La Jolla, CA, USA). Statistical significance between two groups was assessed using an unpaired two-tailed Welch's t-test. Data are shown as median (dot plots) and mean with minimum and maximum (box plots). For all statistically significant comparisons *P* values are displayed on figures and statistical analysis are specified in the figure legends. Biological replicates are specified in the figure legends.

Data availability

The EM maps and atomic models of XPR1$^{\mathrm{InsP6}}$, XPR1$^{\mathrm{InsP6\text{•}Pi}}$ and XPR1$^{\mathrm{TMD}}$ have been deposited in the Electron Microscopy Data Bank and Protein Data Bank, with the accession numbers EMD-68789, EMD-68790, and EMD-68791, and 22ZH.PDB, 22ZI.PDB and 22ZK.PDB, respectively. Materials are available from the corresponding authors on request.

Declarations

Acknowledgments

We would like to thank the staffs at the Advanced Bio-imaging Technology Platform of Guangzhou Laboratory for cryo-EM data collection. We are grateful to professor Jinsai Shang, Dr. Min Zhou, Dr. YongZhi Lu, and Ms. Mei Li for assistance during EM data collection. We thank the Center for Protein Research, and Dr. Jianbo Cao at the Public Laboratory of Electron Microscopy, Huazhong Agricultural University, for technical support. This work was supported by the National Natural Science Foundation of China (32422041), the Fundamental Research Funds for the Central Universities (2662025SKPY008) and the HZAU-AGIS Cooperation Fund (SZYJY2022022). Yong Wang acknowledges the computational support of the Information Technology Center and State Key Lab of CAD&CG at Zhejiang University.

Author contributions

Z.L. conceived and supervised the project. Y.L. and J.Z. designed experiments. Y.L. prepared samples and performed biochemical experiments. J.Z. and L.J. determined the structures. K.L., K.N., H.H., Z.D., J.Z., S.C., X.P., G.B., W.Z. and Y.C. contributed to plasmids constructing, data collection and analysis. Y.W. performed MD analysis. Y.L. and Z.L. wrote the manuscript with help from all authors.

Competing interests

The authors declare no competing interests.

Correspondence and requests for materials should be addressed to Zhu Liu (liuzhu@mail.hzau.edu.cn)

References

1. Jennings ML (2023) Role of transporters in regulating mammalian intracellular inorganic phosphate. Front Pharmacol 14:1163442
2. Kavanaugh MP et al (1994) Cell-surface receptors for gibbon ape leukemia virus and amphotropic murine retrovirus are inducible sodium-dependent phosphate symporters. *Proc. Natl. Acad. Sci. U. S. A.* 91, 7071–7075
3. Olah Z, Lehel C, Anderson WB, Eiden MV, Wilson CA (1994) The cellular receptor for gibbon ape leukemia virus is a novel high affinity sodium-dependent phosphate transporter. J Biol Chem 269:25426–25431
4. Hilfiker H et al (1998) Characterization of a murine type II sodium-phosphate cotransporter expressed in mammalian small intestine. *Proc. Natl. Acad. Sci. U. S. A.* 95, 14564–14569
5. Murer H, Hernando N, Forster I, Biber J (2000) Proximal tubular phosphate reabsorption: molecular mechanisms. Physiol Rev 80:1373–1409
6. Forster IC, Hernando N, Biber J, Murer H (2013) Phosphate transporters of the SLC20 and SLC34 families. Mol Aspects Med 34:386–395

7. Virkki LV, Biber J, Murer H, Forster IC (2007) Phosphate transporters: a tale of two solute carrier families. Am J Physiol -Renal Physiol 293:F643–F654
8. Giovannini D, Touhami J, Charnet P, Sitbon M, Battini JL (2013) Inorganic phosphate export by the retrovirus receptor XPR1 in metazoans. Cell Rep 3:1866–1873
9. Tailor CS, Nouri A, Lee CG, Kozak C, Kabat D (1999) Cloning and characterization of a cell surface receptor for xenotropic and polytropic murine leukemia viruses. *Proc. Natl. Acad. Sci. U. S. A.* 96, 927–932
10. Vaughan AE, Mendoza R, Aranda R, Battini JL, Miller AD (2012) Xpr1 is an atypical G-protein-coupled receptor that mediates xenotropic and polytropic murine retrovirus neurotoxicity. J Virol 86:1661–1669
11. Li X et al (2020) Control of XPR1-dependent cellular phosphate efflux by InsP(8) is an exemplar for functionally-exclusive inositol pyrophosphate signaling. *Proc. Natl. Acad. Sci. U. S. A.* 117, 3568–3574
12. Yao X et al (2017) Analysis of gene expression and functional characterization of XPR1: a pathogenic gene for primary familial brain calcification. Cell Tissue Res 370:267–273
13. Legati A et al (2015) Mutations in XPR1 cause primary familial brain calcification associated with altered phosphate export. Nat Genet 47:579–581
14. Anheim M et al (2016) XPR1 mutations are a rare cause of primary familial brain calcification. J Neurol 263:1559–1564
15. Balck A et al (2021) Genotype-Phenotype Relations in Primary Familial Brain Calcification: Systematic MDSGene Review. Mov Disord 36:2468–2480
16. Bondeson DP et al (2022) Phosphate dysregulation via the XPR1-KIDINS220 protein complex is a therapeutic vulnerability in ovarian cancer. Nat Cancer 3:681–695
17. Akasu-Nagayoshi Y et al (2022) PHOSPHATE exporter XPR1/SLC53A1 is required for the tumorigenicity of epithelial ovarian cancer. Cancer Sci 113:2034–2043
18. Wilson MS, Jessen HJ, Saiardi A (2019) The inositol hexakisphosphate kinases IP6K1 and – 2 regulate human cellular phosphate homeostasis, including XPR1-mediated phosphate export. J Biol Chem 294:11597–11608
19. Li X et al (2024) Homeostatic coordination of cellular phosphate uptake and efflux requires an organelle-based receptor for the inositol pyrophosphate IP8. Cell Rep 43:114316
20. Moritoh Y et al (2021) The enzymatic activity of inositol hexakisphosphate kinase controls circulating phosphate in mammals. Nat Commun 12:4847
21. Lopez-Sanchez U et al (2020) Interplay between primary familial brain calcification-associated SLC20A2 and XPR1 phosphate transporters requires inositol polyphosphates for control of cellular phosphate homeostasis. J Biol Chem 295:9366–9378
22. Wilson MSC, Livermore TM, Saiardi A (2013) Inositol pyrophosphates: between signalling and metabolism. Biochem J 452:369–379

23. Bennett M, Onnebo SMN, Azevedo C, Saiardi A (2006) Inositol pyrophosphates: metabolism and signaling. Cell Mol Life Sci 63:552–564
24. Azevedo C, Saiardi A (2017) Eukaryotic Phosphate Homeostasis: The Inositol Pyrophosphate Perspective. Trends Biochem Sci 42:219–231
25. Wild R et al (2016) Control of eukaryotic phosphate homeostasis by inositol polyphosphate sensor domains. Science 352:986–990
26. Zhang W et al (2025) Structural insights into the mechanism of phosphate recognition and transport by XPR1. Nat Commun 16:18
27. Yan R et al (2024) Human XPR1 structures reveal phosphate export mechanism. Nature 633:960–967
28. Wang X et al (2025) KIDINS220 and InsP8 safeguard the stepwise regulation of phosphate exporter XPR1. Mol Cell 85:3209–3224
29. Lu Y et al (2024) Structural basis for inositol pyrophosphate gating of the phosphate channel XPR1. Science 386:eadp3252
30. Wang Y et al (2025) Structural basis of phosphate export by human XPR1. Cell Res 35:313–316
31. He Q et al (2025) Structural basis of phosphate export by human XPR1. Nat Commun 16:683
32. Chen L, He J, Wang M, She J (2025) Structure and function of human XPR1 in phosphate export. Nat Commun 16:2983
33. Wu H et al (2025) The identification of XPR1 as a voltage- and phosphate-activated phosphate-permeable ion channel. Nat Commun 16:4519
34. Zhu Q, Yaggi MF, Jork N, Jessen HJ, Diver MM (2025) Transport and InsP8 gating mechanisms of the human inorganic phosphate exporter XPR1. Nat Commun 16:2770
35. Scholz-Starke J, Cesca F (2016) Stepping Out of the Shade: Control of Neuronal Activity by the Scaffold Protein Kidins220/ARMS. Front Cell Neurosci 10:68
36. Iglesias T et al (2000) Identification and cloning of Kidins220, a novel neuronal substrate of protein kinase D. J Biol Chem 275:40048–40056
37. Burns D, Berlinguer-Palmini R, Werner A (2024) XPR1: a regulator of cellular phosphate homeostasis rather than a Pi exporter. Pflug Arch: Eur J Physiol 476:861–869
38. Quintans B, Oliveira J, Sobrido M (2018) Primary familial brain calcifications. Handb Clin Neurol 147:307–317
39. Wang H et al (2024) XPR1 promotes ovarian cancer growth and regulates MHC-I through autophagy. Genes Dis 12:101507
40. Abramson J et al (2024) Accurate structure prediction of biomolecular interactions with AlphaFold 3. Nature 630:493–500
41. Zuo P et al (2025) Synergistic activation of the human phosphate exporter XPR1 by KIDINS220 and inositol pyrophosphate. Nat Commun 16:2879

42. Guan Z et al (2023) The cytoplasmic synthesis and coupled membrane translocation of eukaryotic polyphosphate by signal-activated VTC complex. Nat Commun 14:718
43. Punjani A, Rubinstein JL, Fleet DJ, Brubaker MA (2017) cryoSPARC: algorithms for rapid unsupervised cryo-EM structure determination. Nat Methods 14:290–296
44. Wang N et al (2021) Structural basis of human monocarboxylate transporter 1 inhibition by anti-cancer drug candidates. Cell 184:370–383
45. Chen S et al (2013) High-resolution noise substitution to measure overfitting and validate resolution in 3D structure determination by single particle electron cryomicroscopy. Ultramicroscopy 135:24–35
46. Jumper J et al (2021) Highly accurate protein structure prediction with AlphaFold. Nature 596:583–589
47. Emsley P, Cowtan K (2004) Coot: model-building tools for molecular graphics. Acta Crystallogr D 60:2126–2132
48. Adams PD et al (2010) PHENIX: a comprehensive Python-based system for macromolecular structure solution. Acta Crystallogr D 66:213–221
49. Davis IW et al (2007) MolProbity: all-atom contacts and structure validation for proteins and nucleic acids. Nucleic Acids Res 35:W375–W383
50. Barad BA et al (2015) EMRinger: side chain-directed model and map validation for 3D cryo-electron microscopy. Nat Methods 12:943–946
51. Jo S, Kim T, Iyer VG, Im W (2008) CHARMM-GUI: a web-based graphical user interface for CHARMM. J COMPUT CHEM 29(11):1859–1865
52. Huang J, Rauscher S, Nawrocki G et al (2017) CHARMM36m: an improved force field for folded and intrinsically disordered proteins. NAT METHODS 14(1):71–73
53. Vanommeslaeghe K, Hatcher E, Acharya C et al (2010) CHARMM general force field: A force field for drug-like molecules compatible with the CHARMM all-atom additive biological force fields. J COMPUT CHEM 31(4):671–690
54. Hopkins CW, Le Grand S, Walker RC, Roitberg AE (2015) Long-Time-Step Molecular Dynamics through Hydrogen Mass Repartitioning. J CHEM THEORY COMPUT 11(4):1864–1874
55. Abraham MJ, Murtola T, Schulz R et al (2015) GROMACS: High performance molecular simulations through multi-level parallelism from laptops to supercomputers. SOFTWAREX ; 1–2:19–25
56. Tan K, Zhang J, Du Z, Hu J, Liu Z (2025) Inhibition of 53BP1-mediated DNA damage repair by a bacterial effector protein. Fundamental Res 5:1581–1583

Figures

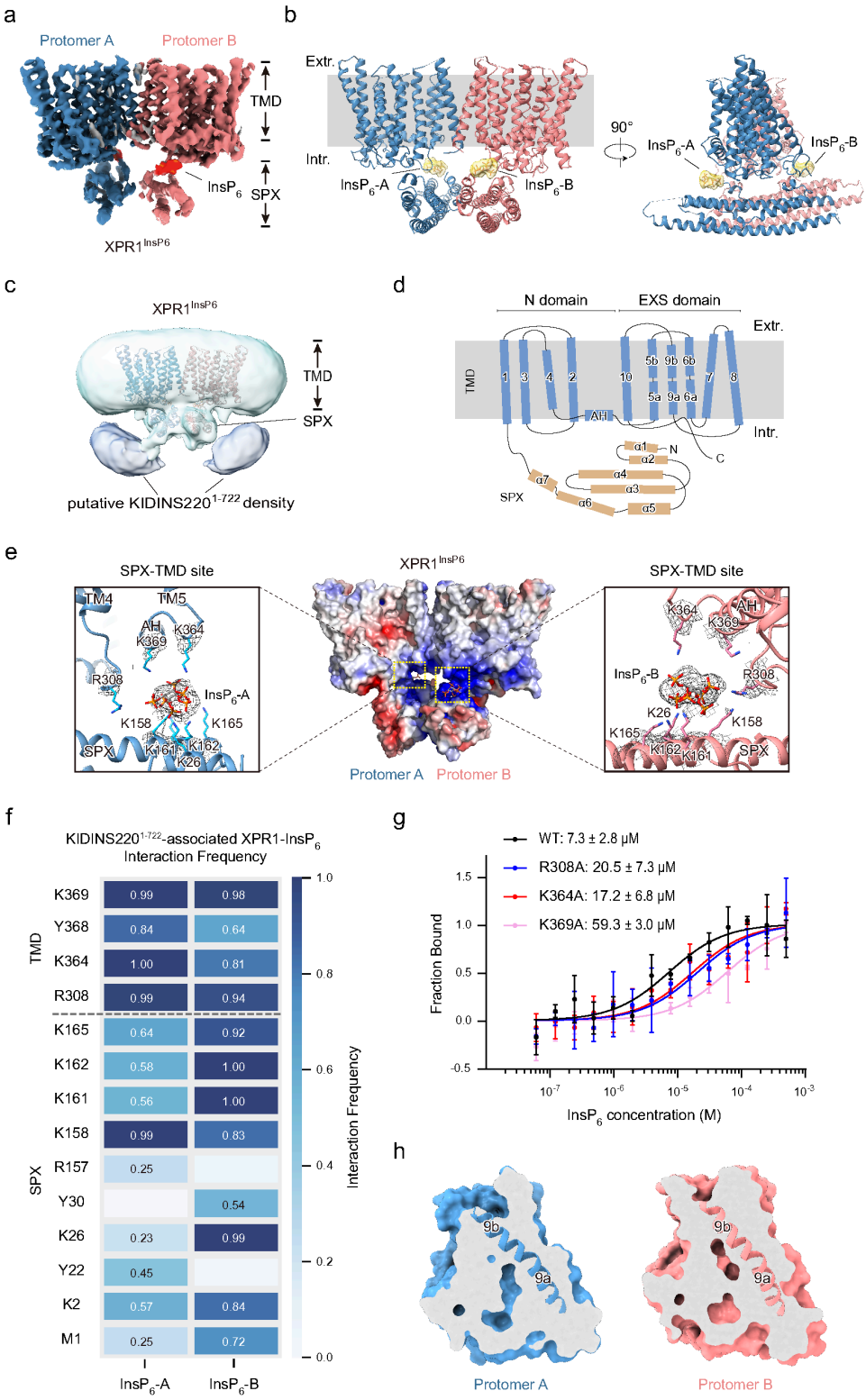


Figure 1

Cryo-EM structure of XPR1 bound to KIDINS220 and $InsP_6$. a, Side view cryo-EM density map of $XPR1^{InsP6}$ dimer. Protomers A (steel blue) and B (light coral) show $InsP_6$-A/B (red) bound within SPX domains beneath the transmembrane region. **b,** Atomic model fitted to cryo-EM density in dual orientations. TMD and SPX domains labeled; $InsP_6$ shown as element-colored sticks within ligand

density (semi-transparent gold). Extracellular (Extr.) and intracellular (Intr.) regions indicated. **c,** Representation of the full XPR1^{InsP6}-KIDINS220$^{1-722}$ complex map at low contour level. Densities: XPR1 (cyan), KIDINS220 (cornflower blue; partial density). **d,** XPR1 topology diagram: TMD (steel blue), SPX domain (light golden brown). **e,** Electrostatic surface representation of XPR1^{InsP6} showing two $InsP_6$ molecules bound at the SPX–TMD interfaces of protomers A and B. Insets highlight the corresponding $InsP_6$-binding sites, where $InsP_6$-A and $InsP_6$-B are coordinated by residues from the SPX domain, TMD, and the amphipathic helix (AH), forming SPX–TMD interaction interfaces. Cryo-EM densities corresponding to the putative $InsP_6$-A and $InsP_6$-B molecules and their interacting residues are shown as gray meshes, contoured at levels of 0.108 and 0.12, respectively, in ChimeraX. **f,** A heatmap summarizes the interaction frequencies from all-atom MD simulations (4 × 1 μs replicates) between XPR1 residues and $InsP_6$-A/B. TMD and SPX residues are separated by a dashed line. Interaction frequency is defined as the fraction of simulation frames in which a given residue contacts the corresponding $InsP_6$ molecule. Darker blue indicates more persistent interactions. **g,** $InsP_6$ binding affinity of the wild-type XPR1–KIDINS220$^{1-722}$ complex (WT) and XPR1 mutants in complex with KIDINS220$^{1-722}$ was determined by microscale thermophoresis. Data from at least three independent measurements were combined and analyzed using MO Affinity Analysis software (NanoTemper Technologies), and fitted to a single binding-site model. The K_d values for $InsP_6$ binding are: wild-type XPR1, 7.3 ± 2.8 μM; R308A mutant, 20.5 ± 7.3 μM; K364A mutant, 17.2 ± 6.8 μM; and K369A mutant, 59.3 ± 3.0 μM. **h,** Cross-sectional surfaces highlighting TM9b closure in both protomers (steel blue: A, light coral: B).

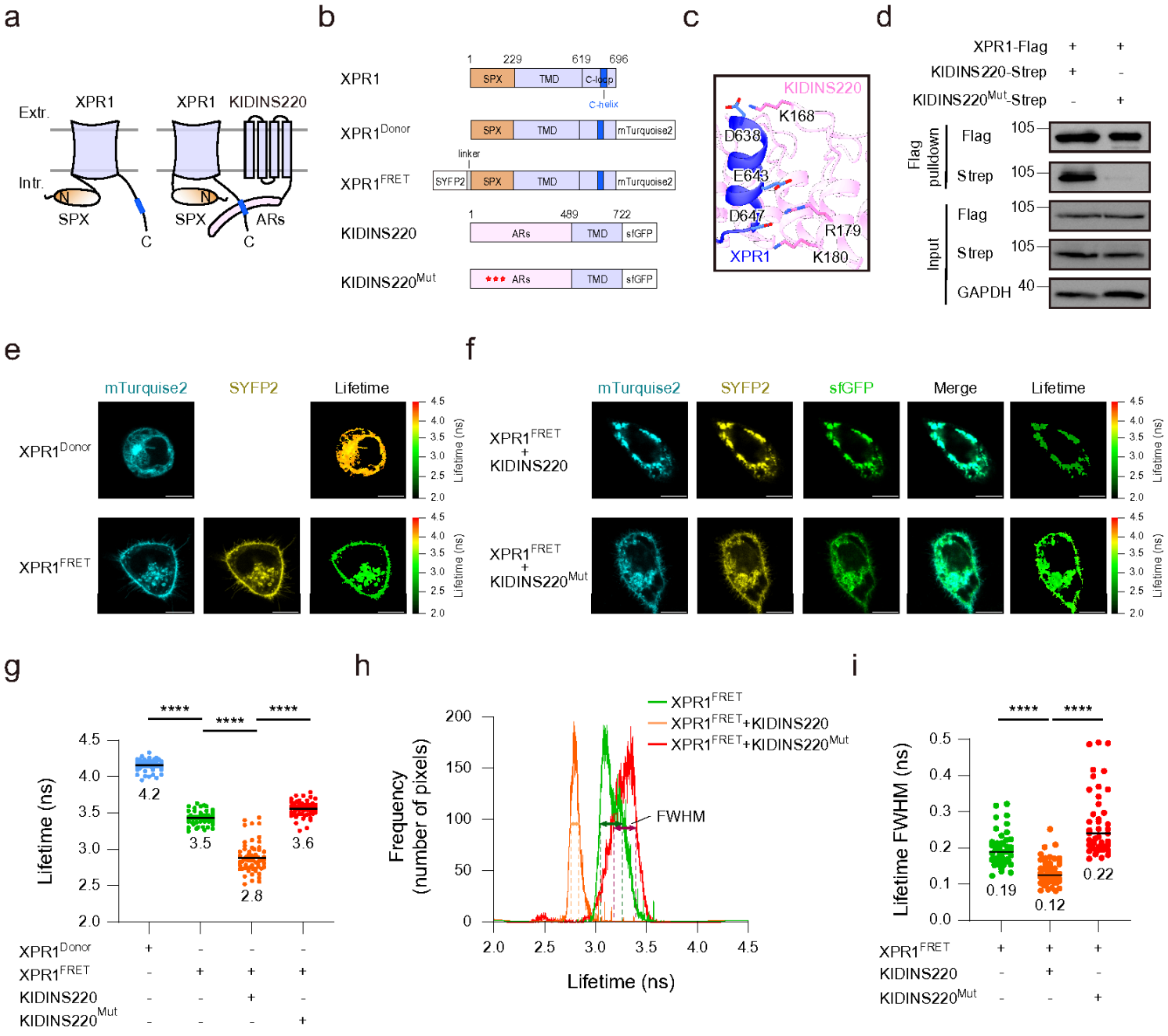


Figure 2

KIDINS220 binding stabilizes compact conformation of XPR1 in living cells. a, Interaction model between KIDINS220 and XPR1. **b,** Schematic representation of the fluorescent protein fusion constructs utilized in this study. Construct schematics: XPR1^{Donor} (C-terminal mTurquoise2), XPR1^{FRET} (N-terminal SYFP2 fused via a GGSGGSGGS linker + C-terminal mTurquoise2), KIDINS220 (including 1-722 residues, C-terminal sfGFP) and charge-reversal mutant KIDINS220^{Mut} (including 1-722 residues, C-terminal sfGFP). Red stars indicate K168E/R179E/K180E mutations in the KIDINS220^{Mut}. **c,** Predicted binding interface showing salt bridges between acidic residues on XPR1 C-terminal helix (Asp638/Glu643/Asp647) and basic residues on KIDINS220 AR domain (Lys168/Arg179/Lys180). **d,** Co-expression and pull-down assays of Flag-tagged XPR1 with Strep-tagged KIDINS220 or KIDINS220^{Mut},

demonstrating abolished KIDINS220-XPR1 interaction upon charge-reversal mutagenesis. GAPDH was used as a loading control to indicate comparable cell input. **e,** Representative FLIM–FRET images of HeLa cells expressing $XPR1^{Donor}$ (top) and $XPR1^{FRET}$ (bottom). Pseudocolor maps indicate donor fluorescence lifetime (τ_D) distribution ranging from 2.0 to 4.5 ns. Scale bars, 10 μm. **f,** Representative FLIM–FRET images of cells co-expressing $XPR1^{FRET}$ with KIDINS220 (top) or $KIDINS220^{Mut}$ (bottom). The sfGFP channel denotes KIDINS220 expression, and merged images show partial co-localization with XPR1. **g,** Quantification of mTurquoise2 fluorescence lifetime. n ≥ 50 cells per group. Dots represent individual cells, and horizontal lines indicate the mean. ****p < 0.0001 (unpaired two-tailed Welch's t-test). **h,** Representative lifetime distribution histograms from individual cells expressing $XPR1^{FRET}$ alone, $XPR1^{FRET}$ + KIDINS220, and $XPR1^{FRET}$ + $KIDINS220^{Mut}$. KIDINS220 shifts the τ_D peak toward shorter lifetimes and narrows the distribution, while $KIDINS220^{Mut}$ largely preserves the broader pattern observed for $XPR1^{FRET}$ alone. The full-width-at-half-maximum (FWHM) of τ_D is indicated for each condition. **i,** Quantification of τD FWHM values derived from the lifetime distributions shown in (H). Dots represent individual cells, and horizontal lines indicate the mean. ****p < 0.0001 (unpaired two-tailed Welch's t-test).

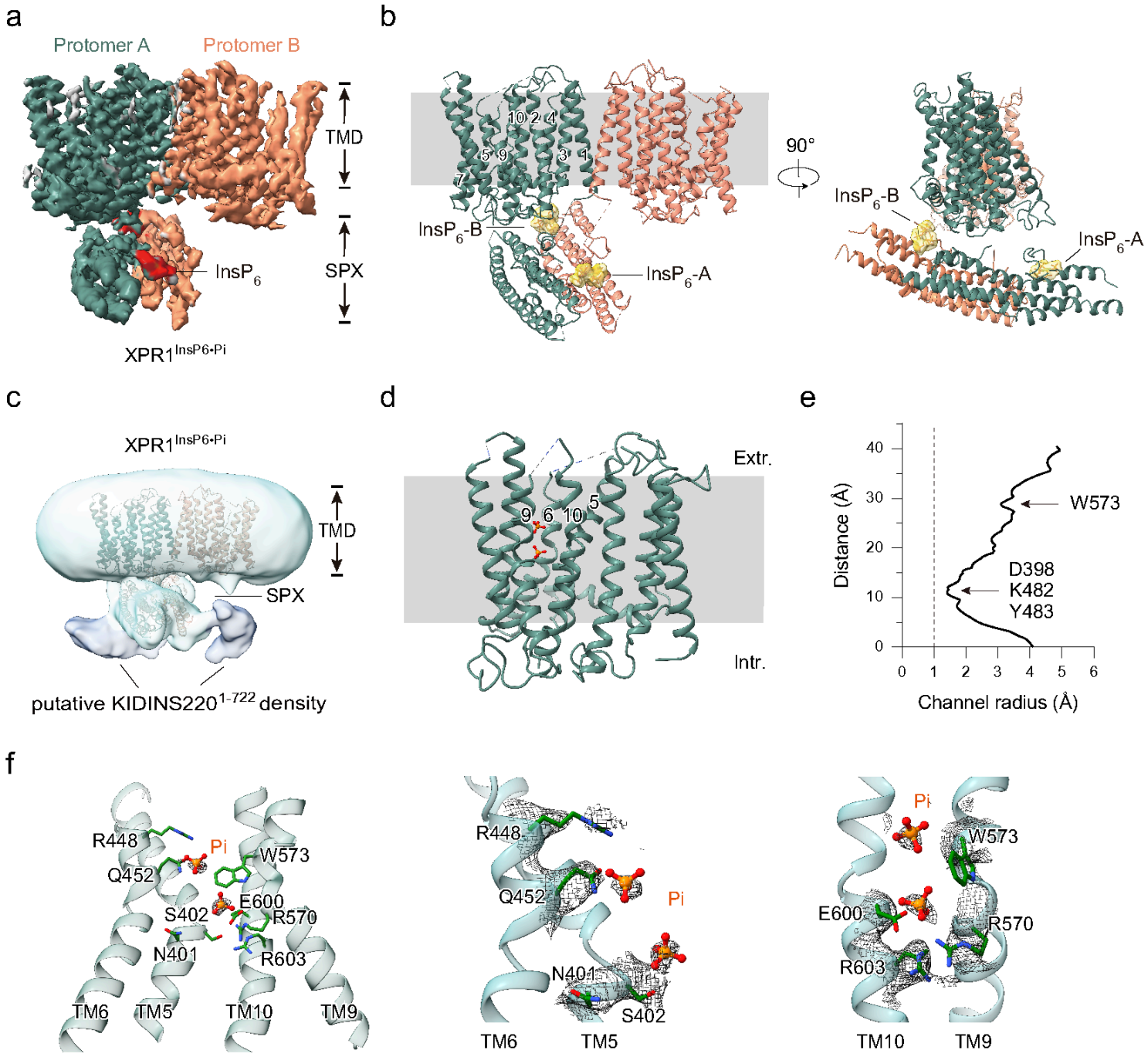


Figure 3

Cryo-EM structure of KIDINS220-associated XPR1 in the presence of $InsP_6$ and phosphate ions. a, Overall cryo-EM density map, designated as $XPR1^{InsP6•Pi}$. The two protomers of XPR1 are shown in teal and orange, respectively. **b,** Atomic model in membrane-plane (left) and side (right) views. $InsP_6$ molecules (sticks) are enclosed by a semi-transparent gold surface. **c,** Low-contour map revealing tenuous KIDINS220 density in this complex (cornflower blue mesh). **d,** Structure of $XPR1^{TMD}$ protomer A. The phosphate ions are shown as sticks. e, Pore radius along the channel. The gray dashed line indicates a radius of 1 Å for water access limit. **f,** Pi translocation cavity, showing key coordinating

residues that line the pathway and are positioned to engage Pi during transport. The putative Pi densities are represented with a contour level of 0.077 in ChimeraX.

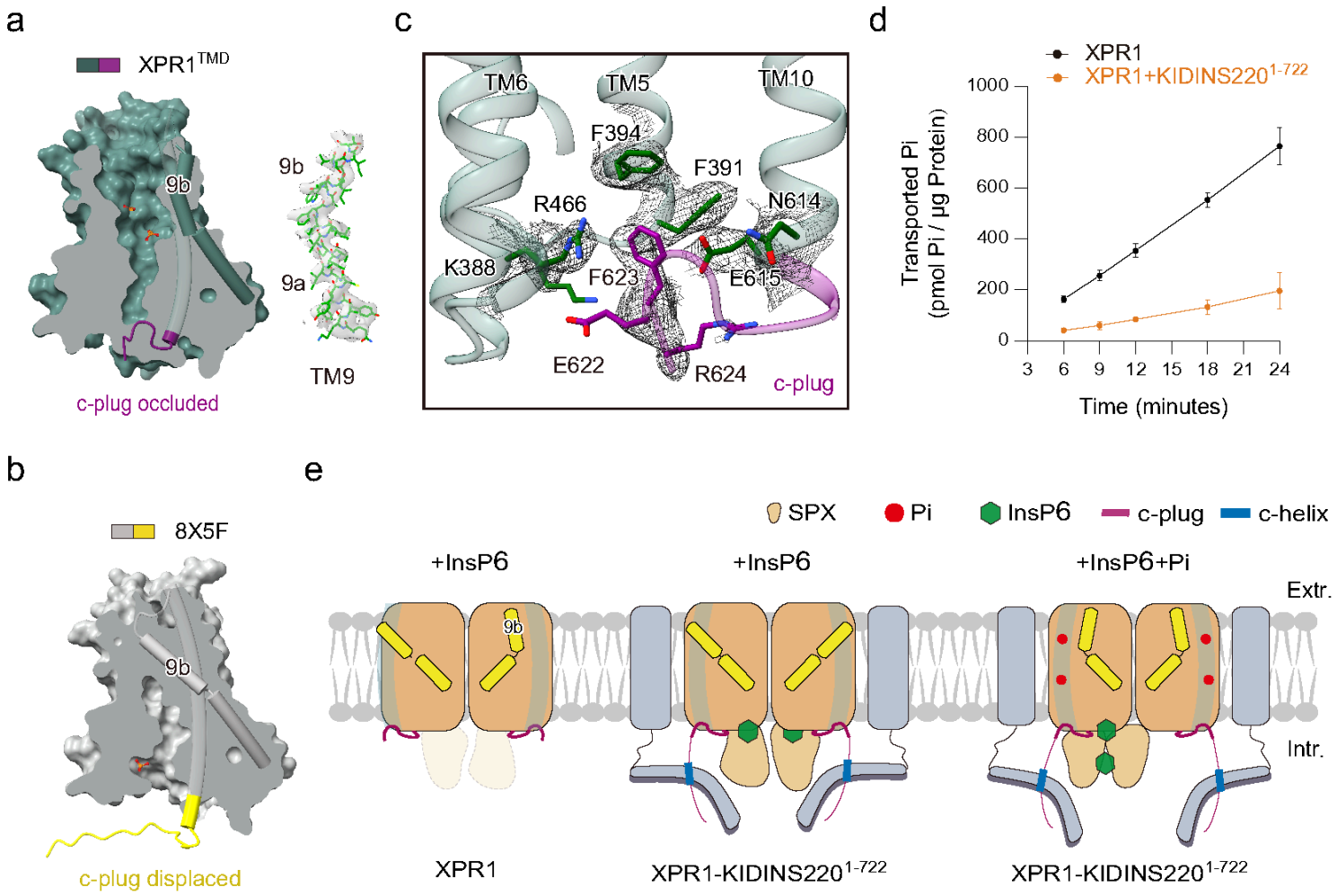


Figure 4

KIDINS220 stabilizes the XPR1 C-plug in an occluded state and attenuates phosphate export. a-b, Surface representations highlighting C-terminal plug conformational states of our C-plug-occluded XPR1^{TMD} strucutre (**a**) and previous reported C-plug-displaced structure (8X5F.PDB) (**b**). The cytoplasmic C-plug is highlighted in purple and yellow, respectively. The bound Pi ions are shown as sticks. The cryo-EM density for TM9 in our structure is shown separately as a gray mesh, contoured at a map level of 0.085 in ChimeraX. **c,** Molecular determinant close-up showing C-plug stabilization network in XPR1^{TMD} structure. The densities are represented with a contour level of 0.077 in ChimeraX. **d,** Quantitative Pi transport kinetics demonstrating KIDINS220-mediated inhibition. The data for XPR1 alone are adapted from our previous report[26], and Pi transport activity of KIDINS220-bound XPR1 was represented as the mean ± SD from three independent experiments. **e,** Proposed model of KIDINS220-mediated inhibition. KIDINS220 docks onto XPR1, allosterically stabilizing both the C-plug occlusion and SPX configuration to lock the transporter in an inactive conformation, preventing phosphate release.

Supplementary Files

This is a list of supplementary files associated with this preprint. Click to download.

- SI20260622.pdf